Nanoscale

RSCPublishing

ARTICLE

Efficient and durable oxygen reduction and evolution of hydrothermally synthesized $La(Co_{0.55}Mn_{0.45})_{0.99}O_{3-\delta}$ nanorod/graphene hybrid in alkaline media

Cite this: DOI: 10.1039/xoxxoooooox

Received ooth January 2012,
Accepted ooth January 2012

DOI: 10.1039/xoxxoooooox

www.rsc.org/

Xiaoming Ge,[a] F. W. Thomas Goh,[a] Bing Li,[a] T. S. Andy Hor,*[ab] Jie Zhang,[a] Peng Xiao,[c] Xin Wang,[c] Yun Zong*[a] and Zhaolin Liu*[a]

The increasing global energy demand and the depletion of fossil fuels have stimulated intense research on fuel cells and batteries. Oxygen electrocatalysis plays essential roles as the electrocatalytic reduction and evolution of di-oxygen are always the performance-limiting factor of those devices relying on oxygen electrochemistry. A novel perovskite with the formula of $La(Co_{0.55}Mn_{0.45})_{0.99}O_{3-\delta}$ (LCMO) is designed from molecular orbital principles. The hydrothermally synthesized LCMO nanorods have unique structural and chemical properties and own high intrinsic activities for oxygen reduction reaction (ORR) and oxygen evolution reaction (OER). The synergic covalent coupling between LCMO and NrGO enhances the bifunctional ORR and OER activities of the novel LCMO/NrGO hybrid catalyst. The ORR activity of LCMO/NrGO is comparable with the state-of-the-art Pt/C catalyst and its OER activity is competitive to the state-of-the-art Ir/C catalyst. LCMO/NrGO generally outperforms Pt/C and Ir/C with better bifunctional ORR and OER performance and operating durability. LCMO/NrGO represents a new class of low-cost, efficient and durable electrocatalyst for fuel cells, water electrolysers and batteries.

Introduction

Fuel cells and batteries attract great interests after the growing concerns on fossil fuel depletion and exacerbated environmental pollution. These devices are required for either mitigating the intermittent nature of renewable energy sources such as solar and wind powers or for end-use such as electric cars and portable electronics. Oxygen electrocatalysis plays essential roles in fuel cells and metal-air batteries as the highly irreversible electrocatalytic oxygen reduction and evolution reactions are always the rate-determining steps of overall electrochemical reactions. Oxygen reduction reaction (ORR) is the cathodic reaction in fuel cells and primary metal-air batteries.[1-3] Oxygen evolution reaction (OER) is the prevailing anodic reaction for regenerative fuel cells, rechargeable metal-air batteries, photocatalytic fuel synthesis, and water electrolysers.[4-6] Instead of separated ORR and OER catalysts, bifunctional electrocatalysts that are catalytically active towards both ORR and OER are preferred for reversible electrochemical devices such as rechargeable metal-air batteries and regenerative fuel cells.[7-10] The state-of-the-art ORR catalysts are those consisting of platinum-based nanocrystals supported on carbon blacks.[11] Unfortunately, platinum-based catalysts behave moderately towards oxygen evolution due to the formation of surface oxide film and the sensitivity to alcohol fuels.[12] Iridium- and ruthenium-based nanostructures are highly efficient OER catalysts but have poor catalytic activity for the ORR.[13] The prohibitive high cost represents another practical hurdle of large scale deployment of noble-metal based catalysts for industrial applications. Nowadays, low-cost and efficient bifunctional catalysts for fuel cells and batteries remain a technical challenge.

The alkaline media provides the opportunity of low-cost materials such as metal oxides as catalyst for alkaline fuel cells, water electrolysers and batteries.[14] First-row transition metal oxides, especially of spinel and perovskite structures,[15-18] are

potential alternatives to noble metal-based counterparts. Perovskite, with the general formulation of ABO_3, consists of corner-shared BO_6 octahedra together with A cations at the corners of its unit cell. The perovskite structure is able to withstand considerable mismatch between the (A–O) and (B–O) bond lengths and accommodate more than one A-site and/or B-site cation species. The great tolerance of lattice mismatch and lattice heterogeneity confers perovskite with unique structural and electronic properties. Shao-Horn et al. designed OER catalysts from σ* antibonding orbital sharing principles and reported $Ba_{0.5}Sr_{0.5}Co_{0.8}Fe_{0.2}O_{3-\delta}$ (BSCF) as an efficient OER catalyst.[18] Recently, the BSCF family is being expanded to $La_{0.8}Sr_{0.2}MnO_{3-\delta}$ decorated $Ba_{0.5}Sr_{0.5}Co_{0.8}Fe_{0.2}O_{3-\delta}$, $La_{0.3}(Ba_{0.5}Sr_{0.5})_{0.7}Co_{0.8}Fe_{0.2}O_{3-\delta}$, $La_{0.58}Sr_{0.4}Fe_{0.8}Co_{0.2}O_3$, and $La_{0.5}Sr_{0.5}Co_{0.8}Fe_{0.2}O_3$ by fine-tuning the lattice doping and surface structure.[19-21] Molecular orbital theories indicated perovskite lanthanum manganite ($LaMnO_3$), lanthanum nickelate ($LaNiO_3$) and lanthanum cobaltite ($LaCoO_3$) are competitive candidates for the ORR.[17] Rotating-disk electrode (RDE) study showed $LaTMO_3$ (TM = Cr, Fe, Ni, Co and Mn) are moderately active for the ORR.[22]

Graphene is a flat monolayer of sp^2 carbon atoms in a two-dimensional honeycomb lattice. Recently, chemically exfoliated graphene and related materials (GRM) have attracted great interests due to their unique structural and electronic properties.[23] Heteroatom doping (oxygen, boron, nitrogen, sulphur, etc.) is an important approach to tailor the chemical properties of graphene. Nitrogen-doped reduced graphene oxide (NrGO) is one of the most widely available GRM and can be regarded as a graphene co-doped with nitrogen and oxygen.[24-25] The spin density and charge distribution of carbon atoms is influenced by the neighbour nitrogen dopants, which induces "hot spots" on the graphene lattice. The activated regions show some activity for ORR and serve as the hot bed to anchor catalysts for versatile applications.[26] Many works have been carried out to grow or attach nanostructured catalysts on NrGO.[27,28] For example, Dai et al. grew spinel nanoparticles on mildly reduced nitrogen-doped graphene oxide and found the covalently coupled spinel–graphene hybrid was highly active for ORR.[29,30] Despite these efforts, material synthesis and studies on efficient perovskite–graphene hybrid for alternating ORR and OER applications are still limited. This is partly because of the difficulty of in situ synthesis of perovskite–graphene hybrid.

Herein, we design a novel perovskite lanthanum manganese cobaltite, $La(Co_{0.55}Mn_{0.45})_{0.99}O_{3-\delta}$ (LCMO), with the e_g electron of 1 (Table S1),† according to Shao-Horn's molecular orbital principles.[17,18] Another feature of LCMO is the 1% B-site vacancy, noting that appropriate lattice vacancy confers good OER activity of oxides.[31] Uniform LCMO nanorods exhibiting high intrinsic activities for ORR and OER were synthesized by a hydrothermal method and relevant heat treatment. To fully unfold the bifunctional capability of LCMO, it was integrated with NrGO by establishing an effective electrically percolating network and leveraging the unique chemical properties of NrGO. The LCMO/NrGO hybrid catalyst exhibited comparable ORR activity with 30 wt.% platinum supported on Vulcan XC-72 carbon (Pt/C) and competitive OER activity to 20 wt.% iridium on Vulcan XC-72 carbon (Ir/C).

Experimental

Materials

Lanthanum nitrate hexahydrate (99.9%) Cobalt(II) nitrate hexahydrate (99.9%), manganese(II) nitrate hexahydrate (99.99%), Nafion 117 solution (5 wt%), sodium hydroxide (99.9%), potassium ferricyanide(III) (99%), and aqueous ammonia were from Sigma-Aldrich. Urea (99%), gold powder (spherical, 0.5-0.8 micron, 99.96+%), 1.0 N standard KOH solution were from Alfa Aesar. Graphene oxide (GO) was from Mitsubishi Chemical Gas. Ultra-high purity oxygen (5N), nitrogen (4N) and hydrogen (5N) were from AIR LIQUIDE. All chemicals were used as received without further purification. 30 wt.% platinum supported on Vulcan XC-72 carbon (Pt/C) was from E-Tek. 20 wt.% iridium on Vulcan XC-72 carbon (Ir/C) was from Premetek. Carbon paper (Spectracarb 2050A) was from Fuel Cell Store. All aqueous solutions were prepared with ultrapure water (>18 MΩ cm) obtained from a Milli-Q plus system (Millipore).

Synthesis of perovskite LCMO nanocrystals and LCMO/NrGO hybrid

In a typical synthesis, 0.350 mmol lanthanum nitrate hexahydrate, 0.191 mmol cobalt nitrate hexahydrate and 0.156 mmol manganese nitrate hydrate were dissolved in 70 mL water. Diluted aqueous ammonia (14 % NH_3 basis) was added dropwise to the solution until the pH value reached 10.5, where the colour of the mixed solution gradually evolved from light pink to pale green. The reaction mixture was allowed to continue stirring in air for 30 min. It was transferred into a 125 ml Teflon-lined stainless steel autoclave (Parr Instrument). The hydrothermal reaction was carried out in an oven at 160 ^oC for 24 h. The product was collected by centrifugation, washed with water and ethanol (volume ratio 1:1) by four times before sending for freeze drying. Finally, the freeze-dried LCMO powders were calcined in air under temperatures from 700 to 1000 ^oC for 3 h. Unless stated explicitly, LCMO was calcined at 810 ^oC for 3 h.

1 mg mL^{-1} GO solution was prepared by diluting the concentrated stock solution and the pH of the suspension was adjusted to 8.0 using aqueous ammonia. In a typical synthesis, 28 mg LCMO was dispersed in 7 mL 1 mg mL^{-1} GO solution together with 28 mL of water. The solution was vigorously stirred for 1 h and 700 mg urea was added. The solution was sonicated for 12 h and further stirred for 1 h to afford a homogeneous mixture. It was transferred to a 47 mL Teflon-lined stainless steel autoclave (Parr Instrument). The hydrothermal treatment was carried out at 170 ^oC for 4 h. The resulted LCMO/NrGO (20 wt.%) hybrid catalyst was collected by centrifugation, washed with water and ethanol for four times and freeze dried. The yield of LCMO/NrGO is ca. 90%.

Materials characterization

Powder X-ray diffraction (XRD) patterns were recorded with a Bruker D2 Phaser using a Cu K_α radiation source. Surface morphology images were taken by a field emission scanning electron microscope (FESEM, JEOL JSM7600F) at an accelerating voltage of 5 KV. Energy-dispersive X-ray (EDX) spectra were recorded by an AZtecSynergy system with X-MAX50 silicon drift detector. Transmission electron microscope (TEM) images were taken by a Philips CM300-FEG at an accelerating voltage of 300 kV. The electron spin resonance (ESR) measurement was carried out using a JEOL FA200 ESR spectrometer at a microwave power of 1 mW and a frequency of 9200 Hz. X-ray photoelectron spectroscopy (XPS) spectra were obtained with a monochromatic Al Kα radiation (VG ESCALAB 200i-XL). Au 4f doublets were used as the internal reference for charge correction. A spectral deconvolution was performed by a curve-fitting procedure based on Lorentzians broadened by a Gaussion using the manufacturer's software (Avantage). Time-of-flight secondary ion mass spectroscopy (TOF-SIMS) depth profiling was performed in dual beam mode using a TOF-SIMS IV instrument (IONTOF GmbH). A 1 keV Ar was used for sputtering and a pulsed 25 keV Bi was used for analysis with detection of positive secondary ions. Charge compensation was achieved using a low energy flood gun.

Electrochemical measurements

All the electrochemical measurements were carried out on an Autolab PGSTAT302N (Metrohm). A three-electrode cell configuration was used with a working electrode of glassy carbon rotating disk electrode (RDE) of 5 mm in diameter, a counter electrode of platinum foil and a reference electrode of Ag/AgCl in 3 M KCl. All electrode potentials were referenced to Ag/AgCl unless stated otherwise. The Ag/AgCl reference electrode was calibrated to reversible hydrogen electrode (RHE) by using a pristine platinum Φ 5mm RDE (Fig. S1).† The glass cell, Ag/AgCl electrode, Pt electrode, glassy carbon electrodes and RDE test rig were from Metrohm. The electrolyte used for all measurements was 0.1 M KOH aqueous solution. To form a catalyst ink, 13 mg of LCMO-based catalysts and 65 µL 5 wt% Nafion solution were dispersed in 2.4 mL of 2.5:1 v/v water/isopropanol mixed solvent for 2 h of sonication. An aliquot of 10 µL of the catalyst ink was applied to a glassy carbon RDE and allowed to dry in air, giving a catalyst loading 0.25 mg cm^{-2}. The catalyst inks of commercial Pt/C and Ir/C were prepared in the following way. 4 mg of catalyst and 13 µL 5 wt% Nafion solution were dispersed in 1 mL of 2.5:1 v/v water/isopropanol mixed solvent for at least 30 min sonication to form a homogeneous ink. 5 µL of the catalyst ink was pipetted onto a glassy carbon RDE, resulting in a catalyst loading 0.1 mg cm^{-2}. Oxygen-saturated electrolyte was prepared by purging O_2 for at least 30 min prior to the start of each experiment. A flow of O_2 was maintained over the electrolyte during the recording of CVs in order to ensure the O_2 saturation. In control experiments, CV measurements were performed in an electrolyte saturated with N_2. The potential sweeping rate was 20 mV s^{-1}. For ORR measurement using RDE, the catalyst-loaded glassy carbon electrode was scanned from 0.2 V to -0.8 V. The potential sweeping rate for ORR and OER was 5 mV s^{-1}. The generated peroxide ion content during ORR was determined by a rotating ring-disk electrode (RRDE) setup with an E7R9 AFE7R9GCPT tip (Pine Instruments). The Pt ring was potentiostated at 0.5 V. The collection efficiency of RRDE was (38.8±0.2)%, as calibrated with deaerated 0.1 M NaOH with 0.01M $K_3Fe(CN)_6$ at a constant ring potential of 0.6 V (Fig. S2).† RDE electrodes were polarized at desired potentials with a rotating rate of 400 rpm for chronopotentiometry and chronoamperometry measurements. For catalyst-loaded carbon-paper air cathode, catalyst inks were prepared by dispersing 85:15 w/w catalyst/Nafion in ethanol. Air cathodes were prepared by the dip coating of catalyst inks on carbon papers and dried under ambient conditions. The mass loading of LCMO/NrGO and Pt/C for ORR was 1 mg cm^2 and 0.25 mg cm^{-2}, respectively. The mass loading of LCMO/NrGO and Ir/C for OER was 6.2 mg cm^{-2} and 1.6 mg cm^{-2}, respectively.

Results and discussion

Typical synthesis methods of perovskite oxides include solid-state reaction,[32] sol-gel,[33] combustion,[34] etc. These methods, however, generally yield submicron particles without well-defined shapes and uniformity. This work introduces a facile and cost-effective approach to synthesize rod-shaped LCMO nanocrystals (hereafter nanorods). LCMO precursors were synthesized from a hydrothermal method using nitrate salts and ammonium hydroxide as precipitating agent and a followed heat treatment. The precursors were calcined at a relatively low temperature of 810 ^oC to form pure-phase perovskite structure and on the meanwhile, to retain the active sites of LCMO. Fig. 1a shows the morphology of synthesized LCMO nanrods with the diameter of 48.5 ± 7.2 nm and the aspect ratio ranging from 3 to 10. Transmission electron spectroscopy (TEM) and high-resolution TEM (HRTEM) images indicate that the highly crystalline LCMO nanorods are composed of low-index and relatively isometric nanocrystals with grain sizes ranging from 19 to 28 nm (Fig. 1b). The perovskite structure emerges after a calcination temperature as low as 710 ^oC but the trace La_2O_3 and $MnCo_2O_4$ impurity phases are eradicated when the calcination temperature reaches 810 ^oC (Fig. S3).† Fig. 1c shows the XRD profile of LCMO calcined at 810 ^oC for 3 h, which crystalizes in orthorhombic structure of Pbnm(62) space group. The unit cell parameters evaluated from a Rietveld refinement are a = 5.5284(17) Å, b = 5.5011(17) Å, c = 7.7248(22) Å and V = 234.93(12) $Å^3$. No exotic peaks other than perovskite reflections are observed. Fig. 1d shows the corner-sharing MO_6 octahedra and the connected oxygen channels of perovskite LCMO. The chemical formula of LCMO is denoted as $La(Co_{0.55}Mn_{0.45})_{0.99}O_{3-\delta}$, as supported by energy dispersive X-ray spectroscopy (Fig. S4).† Vibrating

sample magnetometer showed that LCMO is paramagnetic, which is an indication of unpaired electrons. The unpaired electrons of Co and Mn cations were further detected by the ESR (Fig. S5).† Note that the existence of unpaired electrons would be beneficial to the electrocatalytic activity for ORR and OER.[17,18] TOF-SIMS shows the surface of LCMO is rich of Mn, implying that the surface of LCMO would be terminated by B–O bonds, especially the Mn–O bonds (Fig. S6).†

In this work, the electronic and chemical states of LCMO were tailored by the introduction of NrGO to establish the covalent interfacial interactions between the two components. An engineered LCMO/NrGO (20 wt.%) hybrid material was obtained by a hydrothermal treatment of a graphene oxide solution added with urea and LCMO nanorods as the seed. Urea in the hydrothermal treatment functioned as both the nitrogen source and the reducing agent for the formation of NrGO. XPS results indicate 4.8 at. % nitrogen in NrGO where 63 % is pyrrolic and 37 % is pyridinic (Fig. S7).† The D-band at 1349 cm^{-1} is associated with the defective and disordered graphitic planes. The G-band at 1589 cm^{-1} is related to the E_{2g} vibration mode of sp^2 carbon domains and is an index of degree of graphitization. The intensity ratio of D-band and G-band (I_D/I_G) of NrGO is 0.99. The high I_D/I_G ratio is ascribed to the structural defects caused by N doping in the graphene sheets (Fig. S8).† The characteristic morphology of LCMO nanorods is retained after the hydrothermal hybridization treatment of LCMO and NrGO. LCMO nanorods and NrGO nanoplatelets are evenly distributed in LCMO/NrGO, as observed from the surface morphology and the elemental mapping characterization (Fig. 2a and Fig. S9).† No exotic reflections exist in the XRD pattern of LCMO/NrGO and all the reflections of LCMO/NrGO coincide with those of LCMO (Fig. 2b). These results lead support a successful synthesis of homogenous and impurity-free LCMO/NrGO hybrid.

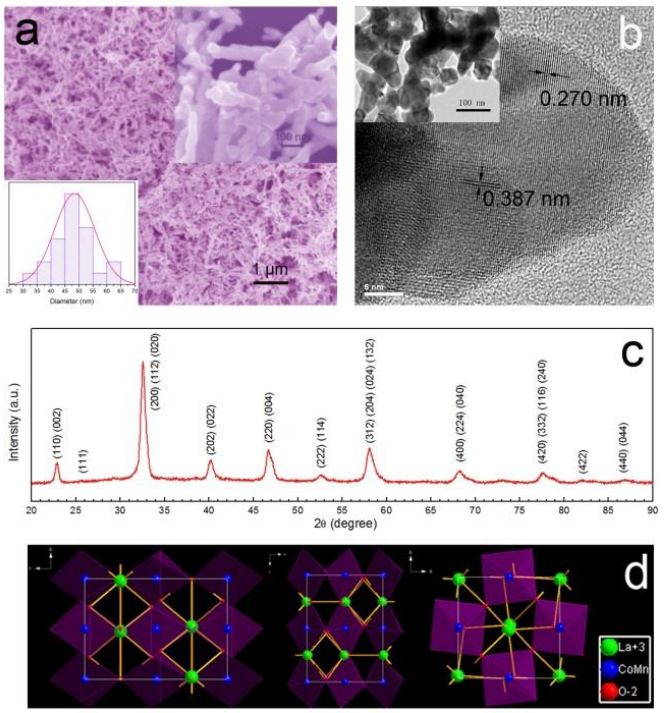

Fig. 1 (a) SEM images of LCMO nanorods. The upper right inset shows LCMO in high magnification. The lower left inset shows the histogram of the diameter of LCMO nanorods. (b) HRTEM and TEM (upper left inset) images of LCMO nanorods. (c) XRD pattern and (d) the structure visualization of LCMO.

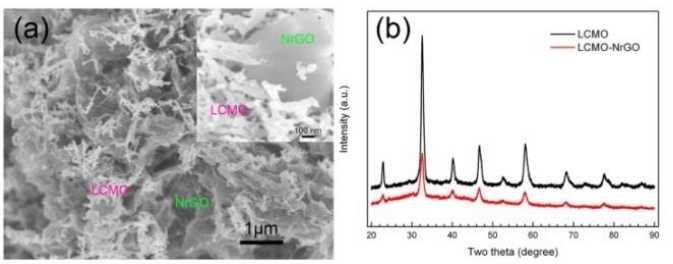

Fig. 2 (a) SEM image of LCMO/NrGO hybrid catalyst. The upper right inset shows LCMO/NrGO in high magnification. (b) XRD patterns of LMCO and LCMO/NrGO.

XPS using Au 4f doublet as reference was employed to extensively study the chemical states of LCMO and the coupling effect between LCMO and NrGO. Fig. 3a–3c show the fitted high-resolution Mn 2p, Co $2p_{3/2}$ and La 3d XPS spectra of LCMO/NrGO and LCMO, and the survey spectra are given in Fig. S10.† Compared to LCMO, the binding energy of Mn^{4+} $2p_{3/2}$ (BE_{Mn4+}) of LCMO/NrGO gains 0.2 eV while BE_{Mn3+} remains unchanged (Fig. 3a). The Mn^{3+} content of the Mn^{3+}/Mn^{4+} redox couple is increased from 21.6 % to 40.8 % (Table S2).† Mn^{3+} ($3d^4$) in perovskite structure is of high spin (H.S.) state and has the electronic configuration $t_{2g}^3e_g^1$,[35-37] cf. $t_{2g}^3e_g^0$ of Mn^{4+} ($3d^3$). The partially filled e_g orbital with 1 e_g electron was beneficial for the oxygen electrode reaction

activities.[17-18] The positive peak shift is more pronounced for Co cations, i.e. 0.3 eV for Co^{2+} ($3d^7$, H.S., $t_{2g}^5e_g^2$)[38,39] and 0.1 eV for Co^{3+} ($3d^6$, intermediate spin, $t_{2g}^5e_g^1$) (Fig. 3b),[40-43] and the Co^{2+} content of the Co^{2+}/Co^{3+} redox couple is decreased from 63.8% to 58.7% (Table S2).† The molecular orbital sharing between the B-site of perovskite and NrGO gives the rise of BE of both Mn and Co, which are observed in the XPS spectra. La 3d has additional satellite and shake-up peaks adjacent to the core level peak. The binding energy separation between satellite and main peak of La $3d_{5/2}$ ($\Delta BE_{3d5/2}$) and the satellite-to-main-peak intensity (S/M) ratio are typical descriptors of the La–O covalent bonding. A larger $\Delta BE_{3d5/2}$ and a larger S/M ratio correspond to stronger La–O covalent bonding chatacteristic.[44,45] The $\Delta BE_{3d5/2}$ and the S/M ratio of La $3d_{5/2}$ are decreased from 4.4 eV and 0.87 of LCMO to 4.2 eV and 0.74 of LCMO/NrGO (Fig. 3c and Table S2),† respectively, both indicating the reduced covalency character of La–O bonding. It is proposed that some localized electronic sharing between La cation and NrGO leads to the populated electron cloud density around A-site of perovskite and subsequently, the decreased $\Delta BE_{3d5/2}$. The (Co + Mn)/La and Mn/Co ratio of LCMO is 1.41 and 2.67, respectively. The XPS results further confirm the accumulation of B cations and the dominance of Mn on LCMO surfaces, in accordance with the TOF-SIMS result (Fig. S6).† While the A/B stoichiometry of ABO_3 structure is somewhat restored after the hybridization between LCMO and NrGO, the surface accumulation of Mn becomes prominent as reflected from the high Mn/Co ratio of 4.42. The octahedral Mn cation sites are conceived to be beneficial for oxygen electrode reactions.[31] Fig. 3d shows fitted O 1s spectra of LCMO/NrGO, NrGO and LCMO, where Scan A is from LCMO, Scan C is from NrGO and Scan B is of mixed character. Figures 3e shows the fitted C 1s spectra of LCMO/NrGO and NrGO, where Scans A, B and C are ascribed to C=C, C=N and C–N bonds, respectively.[46] Fig. 3f show the fitted N 1s spectra of LCMO/NrGO and NrGO, respectively. As observed in Fig. 3d–3e and Table S3,† BE of O 1s, C 1s and N 1s of LCMO/NrGO are ca. 0.1–0.3 eV smaller than those of LCMO and NrGO, which is coincident with the gain of BE of La, Co and Mn cations of LCMO/NrGO. This phenomenon is conceivable because of the molecular orbital sharing and the shift of electron cloud from the metallic cations to the light ~~little~~ elements, another evidence of the covalent coupling between LCMO and NrGO of LCMO/NrGO.

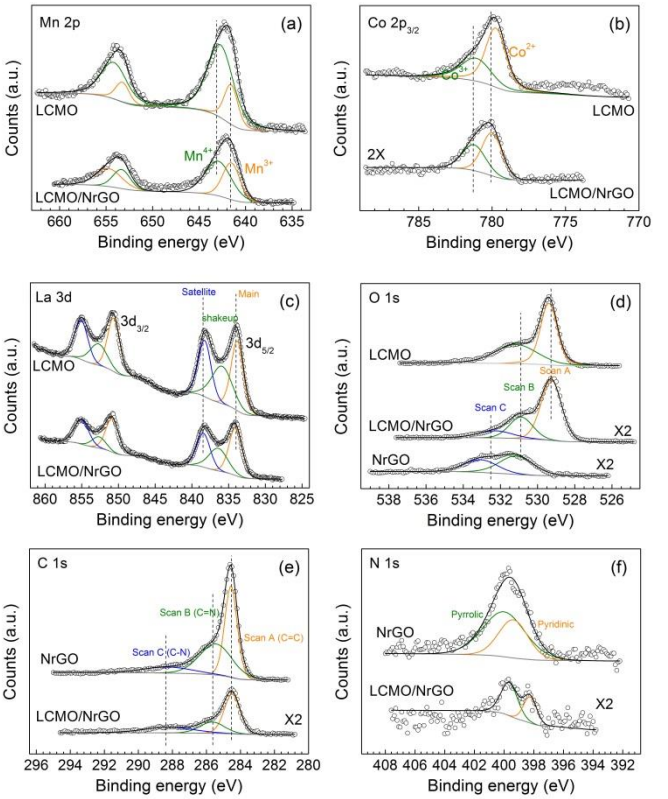

Fig. 3 (a) fitted Mn 2p high-resolution X-ray photoelectron spectra of LCMO/NrGO and LCMO. (b) fitted Co $2p_{3/2}$ high-resolution spectra of LCMO/NrGO and LCMO. (c) fitted La 3d high-resolution spectra of LCMO/NrGO and LCMO. (d) fitted O 1s high-resolution spectra of LCMO/NrGO, LCMO and NrGO. (e) fitted C1s high-resolution spectra of LCMO/NrGO and NrGO. (f) fitted N 1s high-resolution spectra of LCMO/NrGO and NrGO.

The electrocatalytic behaviours of LCMO, LCMO/NrGO, NrGO and the benchmark Pt/C and Ir/C towards ORR ($O_2 + 2H_2O + 4e^- \rightarrow 4\ OH^-$) and OER ($4\ OH^- \rightarrow O_2 + 2H_2O + 4e^-$) were investigated by half-cell testing with the catalyst-loaded glassy carbon RDE as working electrode. The electrolyte was 0.1 M KOH aqueous solution. All electrode potentials are referenced to Ag/AgCl in 3 M KCl reference electrode, which was calibrated with reversible hydrogen electrode (Fig. S1).† Cyclic voltamograms (CVs) in N_2-saturated electrolyte only gives capacitive background currents so that the LCMO-based catalysts and NrGO are electrochemically stable in the electrolyte. CVs in O_2-staurated electrolyte clearly illustrate more positive ORR onset potential of LCMO/NrGO than bare LCMO and NrGO. The oxygen reduction current of LCMO/NrGO is even higher than Pt/C (Fig. 4a). The oxygen reduction peak potential and peak current of LCMO/NrGO are 136 mV more positive and 6% larger than those of Pt/C counterpart. Full-range CVs further confirm LCMO/NrGO as a good bifunctional catalyst towards ORR and OER with competitive ORR activity against Pt/C and comparable OER activity against Ir/C (Fig. S11).† As shown in Fig. 4b, the oxygen reduction current of LCMO emerges ca. -0.01 V but the increase of current is very slow. This phenomenon implies good intrinsic ORR activity of LCMO but the reaction kinetics of

ORR is impeded due to certain constraints such as poor electrical conductivity and electrode architecture. To facilitate the reaction kinetics, LCMO was integrated with NrGO to form a LCMO/NrGO hybrid material. The RDE polarization curves and the associated differential polarization curves (di/dV curves) reveal that the ORR onset potential of LCMO/NrGO and mechanically mixed LCMO and NrGO (LCMO+NrGO) is both -0.025 V, cf. -0.016 V of Pt/C. At -0.8 V, LCMO/NrGO, LCMO+NrGO and Pt/C attain the diffusion-limiting current density (j_L) of –6.64, –6.57 and –5.98 mA cm^{-2}, respectively. The half-wave potential ($E_{½}$) of the ORR voltammogram of LCMO/NrGO is –0.184 V, cf. –0.269 V of LCMO+NrGO. Note that LCMO+NrGO could not afford strong hybrid coupling between the two components, so that the electrocatalytic kinetics as well as j_d are inferior to those of LCMO/NrGO. This confirms the importance of covalent hybrid coupling for outstanding electrocatalytic performance. While $E_{½}$ of the ORR voltammogram of LCMO/NrGO is 16 mV more negative than Pt/C, the peak current density of the associated di/dV ~ V curve, di/dV_{max}, is 48.7 mA cm^{-2} V^{-1} as compared to 37.1 mA cm^{-2} V^{-1} of Pt/C. It is worth to highlight that the di/dV ~ V curve gives good resolution of electric current signals for the mixed kinetic- and diffusion-limiting region of the ORR voltammograms. The CV and RDE results clearly demonstrate better oxygen reduction reaction kinetics of LCMO/NrGO than Pt/C (Fig. 4b).

To further understand the reaction mechanisms of ORR, Koutecky–Levich (K–L) plots were generated from capacitive-corrected RDE voltammograms with RDE rotating rates from 400 to 2500 rpm and electrode potentials from -0.30 V to -0.70 V. The least squares fitted slopes were used to calculate the number of electrons transferred (n) during ORR on the basis of the Koutecky-Levich equation:

$$1/J = 1/J_L + 1/J_K = 1/(B\omega^{1/2}) + 1/J_K \quad (1)$$

$$B = 0.2nFC_0(D_0)^{2/3}\upsilon^{-1/6} \quad (2)$$

$$J_K = nFkC_0 \quad (3)$$

where J is the measured current density and J_K is the kinetic-limiting current density. ω is the angular velocity (rpm), n is the number of transferred electrons, F is the Faraday constant, C_0 is the bulk concentration of O_2 (1.21 mol m^{-3} in 0.1 M KOH),[47] D_0 is the diffusion coefficient of O_2 (1.87 × 10^{-9} m^2 s^{-1} in 0.1 M KOH), υ is the kinematic viscosity of the electrolyte (10^{-6} m^2 s^{-1} in 0.1 M KOH),[48] and k is the electron-transfer rate constant. The electron-transfer numbers (n) obtained from K–L plots are 3.87 ± 0.02 of LCMO/NrGO (Fig. 4c), 3.86 ± 0.10 of LCMO+NrGO (Fig. S12), 3.94 ± 0.11 of LCMO (Fig. S13), and 2.67 ± 0.19 of NrGO (Fig. S14).† The ORR on LCMO proceeds through a pseudo four-electron reaction pathway while the ORR on NrGO mainly favours a two-electron reaction pathway. The n values of LCMO/NrGO and LCMO+NrGO indicate a mixed four-electron and two-electron pathways of ORR. To verify the ORR catalytic activity, a RRDE experiment was carried out to monitor the formation of peroxide ions (HO_2^-) and n during the ORR according to Eqs. 4 and 5:[49,50]

$$X_{peroxide} = 2I_R/(N^*I_D+I_R) \quad (4)$$

$$n = 4I_D/(I_D+I_R/N) \quad (5)$$

Fig. 4d shows the RRDE voltammogram of LCMO/NrGO in alkaline solution. The measured HO_2^- yields are below 10% for LCMO/NrGO over the potential range from –0.2 V to –0.8 V, giving an n value ranging from 3.96 to 3.82 (inset of Fig. 4d). This is consistent with the results derived from the K–L plots of RDE measurements, further confirming a dominating pseudo four-electron reaction pathway of LCMO/NrGO.

Fig. 5 shows the RDE polarization curves and the associated di/dV curves for OER of LMCO/NrGO, LCMO+NrGO, Ir/C, LCMO, NrGO and Pt/C. The OER onset potential of LCMO/NrGO is around 0.45 V, only ca. 50 mV less active than Ir/C. The potentials of LCMO/NrGO and Ir/C at 10 mA cm^{-2}, a current density required to achieve a water splitting efficiency of 10 % with one-sun illumination for solar-to-fuel conversion,[51,52] are 0.787 V and 0.737 V, respectively. Impedance spectroscopy shows that the polarization resistances (R_p) of LCMO/NrGO, LCMO and Pt/C are ca. 200, 1200 and 1700 Ω cm^2 C under 0.6 V (Fig. S15).† Electrocatalytic activity of bifunctional catalyst is commonly described by the potential gap (ΔE) between ORR and OER potentials at current densities of practical significance. A smaller ΔE means a greater "round-trip" efficiency for oxygen electrocatalysis. For ΔE given in this work, ORR current density and OER current density are selected as -3 mA cm^{-2} and 10 mA cm^{-2}, respectively. ΔE of LCMO/NrGO is 0.960 V (cf. 1.086 V of Ir/C), which is competitive to those state-of-the-art bifunctional catalysts as reported in literature,[9,51,53,54] as listed in Table S4.† The salient electrocatalytic performance of LCMO/NrGO would result from the intrinsic activity of perovskite LCMO, the efficiently established percolating NrGO network for electrical conduction and the mechanical and chemical coupling between the LCMO and NrGO components.

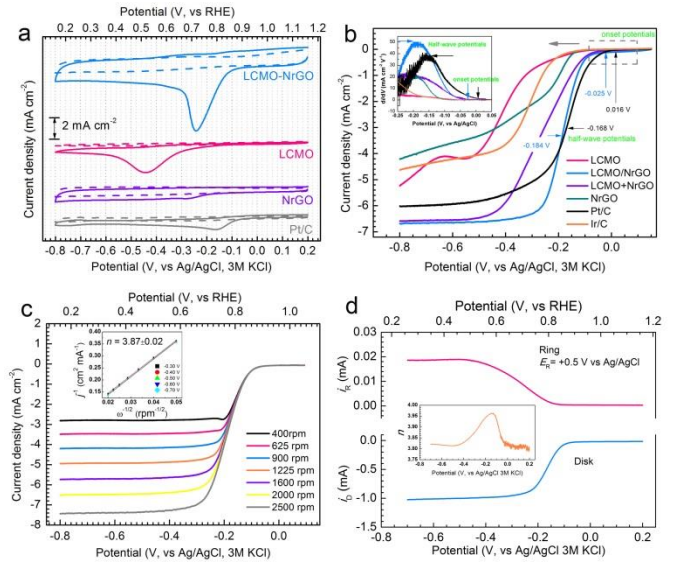

Fig. 4 (a) CV curves of LMCO/NrGO, LCMO, NrGO and Pt/C (O_2-saturated, solid line; N_2-saturated, dashed line). (b) RDE oxygen reduction polarization curves of LMCO/NrGO, LCMO+NrGO, LCMO, NrGO, Pt/C and Ir/C under a rotating rate of 2000rpm in O_2-saturated 0.1 M KOH. The inset shows the corresponding d*i*/d*V* curves. (c) capacitive-corrected RDE oxygen reduction polarization curves of LCMO/NrGO in O_2-saturated 0.1 M KOH and under various rotating rates. The inset shows the corresponding K–L plots. (d) Voltammograms of LCMO/NrGO measured with RRDE in O_2-saturated 0.1 M KOH. The inset shows the corresponding electron transfer number at various potentials.

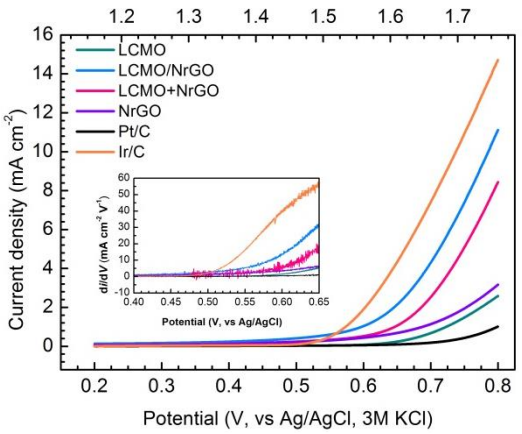

Fig. 5 RDE oxygen evolution polarization curves of LMCO/NrGO, LCMO+NrGO, LCMO, NrGO, Pt/C and Ir/C under a rotating rate of 2000rpm. The inset shows the corresponding d*i*/d*V* curves.

Apart from high ORR and OER activities, the durability of electrocatalysts is crucial for the cycle life of electrochemical energy conversion and storage devices. LCMO/NrGO and the benchmark Pt/C and Ir/C were evaluated by chronoamperometry ($i \sim t$) and chronopotentiometry ($V \sim t$) techniques. Under chronoamperometric polarization of –0.6 V, the degradation rate of the oxygen reduction current of LCMO/NrGO is 2.45% h^{-1}, 11% lower than that of Pt/C (Fig. S16).† The degradation rates of electric potential of LCMO/NrGO at polarizations of –0.1 and –1 mA cm^{-2} are one order of magnitude lower than those of Pt/C (Fig. S17 and Fig. 18).† The chronoamperometry and chronopotentiometry results prove LCMO/NrGO as a more durable ORR electrocatalyst than Pt/C. LCMO/NrGO exhibits an initial passivation stage before the stable OER plateau. As this passivation stage does not occur for the case of LCMO, it is possible due to the reduced surface area and/or structural reconstruction of NrGO of LCMO/NrGO under oxygen evolution conditions.[55] The durability of LCMO/NrGO is further evident from the similar FE-SEM and TEM morphology images of LCMO/NrGO before and after 16-hour chronopotentiometry at –1 mA cm^{-2} and under 400 rpm, (Fig. S19 and S20).† The degradation rate of electrical potential of LCMO/NrGO is 3 times smaller than that of Ir/C, when subjected to chronopotentiometric polarization at 0.1 mA cm^{-2} under OER mode (Fig. S21).†

The operating durability of electrocatalysts towards ORR and OER was further evaluated by half-cell testing of more practical catalyst-loaded air cathodes. Air cathodes were fabricated by anchoring the electrocatalysts onto carbon fibre paper with Nafion as binder. As expected, the blank carbon paper itself showed little catalytic activity. High oxygen reduction kinetics of LCMO/NrGO is evident from Fig. 6a. The electric potential of LCMO/NrGO is -0.419 V under an oxygen reduction current of -20 mA cm^{-2}, 64 mV more active than Pt/C. The OER operating potential of LCMO/NrGO is 0.718 V (cf. 0.686 V of Ir/C), under an oxygen evolution current of 10 mA cm^{-2} (Fig. 6b). The LCMO/NrGO air cathode degrades with a rate of 0.33 mV h^{-1} when polarized under –10 mA cm^{-2} in ORR mode, a degradation rate that is one order of magnitude lower than that of Pt/C (Fig. 6c). XRD, XPS and FE-SEM results indicated that the perovskite structure, the Mn^{3+}/Mn^{4+} redox couple and the surface morphology of LCMO/NrGO air cathode are well retained after the chronopotentiometric degradation test at –10 mA cm^{-2} for 48 h (Fig. S22 to S24).† The degradation rate of the operating potential of LCMO/NrGO is 14.8 mV h^{-1} under the polarization of 5 mA cm^{-2} in OER mode, 34 % lower than that of Ir/C (Fig. 6d). The chronoamperometry and chronopotentiometry results prove LCMO/NrGO as a durable bifunctional catalyst for both ORR and OER. The stable perovskite structure, high crystallinity and the nanorod morphology of LCMO, which are created after heat treatment at elevated temperatures, are beneficial to the low degradation rate of LCMO-based electrocatalysts. Apart from the coupling effect between NrGO and LCMO, the well-dispersed NrGO helps to prevent particle agglomeration and to retain the accessible surface area of the catalysts. These synergic effects would contribute to the salient operating durability of LCMO/NrGO air cathodes.

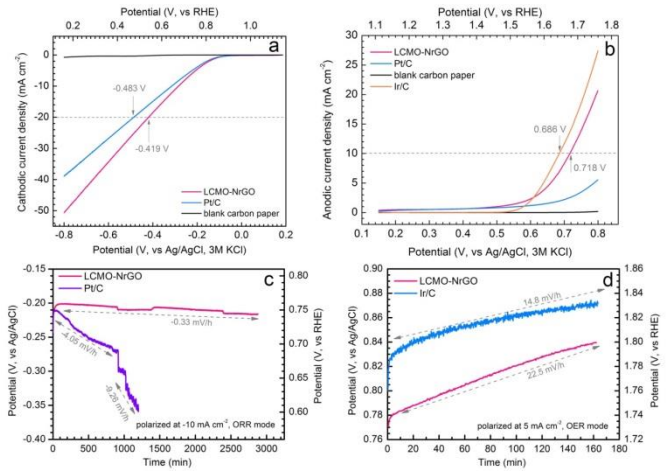

Fig. 6 (a) oxygen reduction polarization curves of LCMO/NrGO, Pt/C and Ir/C loaded on carbon fibre papers. (b) oxygen evolution polarization curves of LCMO/NrGO, Ir/C, LCMO and Pt/C loaded on carbon fibre papers. (c) chronopotentiometric responses of LCMO/NrGO and Pt/C loaded on carbon fibre papers. (d) chronopotentiometric responses of LCMO/NrGO and Ir/C loaded on carbon fibre papers. The electrolyte is O_2-saturated 0.1 M KOH solution.

Conclusions

A novel perovskite $La(Co_{0.55}Mn_{0.45})_{0.99}O_{3-\delta}$ (LCMO) nanorods was designed and synthesized by hydrothermal method for fuel cell, water electrolyser, and battery applications. The surface of highly crystalline LCMO nanorods is rich of transition metal cations, especially Mn cations. LCMO owns high intrinsic activity towards oxygen electrode reactions. RDE and RRDE experiments show that ORR proceeds through a pseudo four-electron reaction pathway on the LCMO surface. By leveraging the synergic covalent coupling effect between oxides and nanocarbon, a novel hybrid electrocatalyst consisting of LCMO and NrGO (LCMO/NrGO) was explored and developed as bifunctional catalyst for ORR and OER. The electrocatalytic activity of LCMO/NrGO for ORR and OER was benchmarked with state-of-the-art fuel cell catalysts, Pt/C and Ir/C. LCMO/NrGO exhibited impressive ORR onset potential, oxygen reduction kinetics in terms of half-wave potential, di/dV_{max}, and n value, OER onset potential and oxygen evolution currents in aqueous alkaline media. LCMO/NrGO generally outperforms Pt/C and Ir/C with better bifunctional ORR/OER performance and operating durability. We have succeeded in developing low-cost, efficient and durable electrocatalysts for alkaline fuel cells, water electrolysers and batteries.

Acknowledgements

This research was supported by the Advanced Energy Storage Programme (IMRE/12-2P0503 and IMRE/12-2P0504), Institute of Materials Research and Engineering (IMRE) of the Agency for Science, Technology and Research (A*STAR), Singapore. The authors are grateful to Guojun Du for TEM observation, Raymond Gan Ching Ruey (IMRE) for magnetic measurement, Doreen Lai Mei Ying (IMRE) and Debbie Seng Hwee Leng for TOF-SIMS depth profiling, and Zheng Zhang (IMRE) and June Ong Lay Ting (IMRE) for XPS characterization.

Notes

[a] Institute of Materials Research and Engineering (IMRE), A*STAR (Agency for Science, Technology and Research), 3 Research Link, Singapore 117602, Republic of Singapore. Email:zl-liu@imre.s-star.edu.sg; y-zong@imre.a-star.edu.sg; andyhor@imre.a-star.edu.sg
[b] Department of Chemistry, National University of Singapore, 3 Science Drive 3, Singapore 117543, Republic of Singapore.
[c] School of Chemical and Biochemical Engineering, Nanyang Technological University, 62 Nanyang Drive, Singapore 637459, Republic of Singapore.

Electronic Supplementary Information (ESI) available: Figure S1 to S24, Table S1 to S4. See DOI: 10.1039/b000000x/

References

1. J. Xiao, C. Chen, J. Xi, Y. Xu, F. Xiao, S. Wang and S. Yang, *Nanoscale*, 2015, DOI: 10.1039/C4NR05917D.
2. Y. Zhai, C. Zhu, E. Wang and S. Dong, *Nanoscale*, 2014, **6**, 2964.
3. F. Y. Cheng, T. R. Zhang, Y. Zhang, J. Du, X. P. Han and J. Chen, *Angew. Chem., Int. Ed.*, 2013, **52**, 2474.
4. L. Zeng, T. S. Zhao and L. An, *J. Mater. Chem. A*, 2015, **3**, 1410.
5. V. M. Dhavale, S. S. Gaikwad, L. George, R. N. Devi and S. Kurungot, *Nanoscale*, 2014, **6**, 13179.
6. M. Gong, Y. G. Li, H. L. Wang, Y. Y. Liang, J. Z. Wu, J. G. Zhou, J. Wang, T. Regier, F. Wei and H. J. Dai, *J. Am. Chem. Soc.*, 2013, **135**, 8452.
7. P. Manivasakan, P. Ramasamy and J. Kim, *Nanoscale*, 2014, **6**, 9665.
8. M. Prabu, K. Ketpang and S. Shanmugam, *Nanoscale*, 2014, **6**, 3173.
9. D. Wang, X. Chen, D. G. Evans and W. Yang, *Nanoscale*, 2013, **5**, 5312.
10. H. Zhang, H. Qiao, H. Wang, N. Zhou, J. Chen, Y. Tang, J. Li and C. Huang, *Nanoscale*, 2014, **6**, 10235.
11. G. X. Zhang, S. H. Sun, M. Cai, Y. Zhang, R. Y. Li and X. L. Sun, *Sci. Rep.*, 2013, **3**, 8.
12. S. Y. Shen, T. S. Zhao, J. B. Xu and Y. S. Li, *Energy Environ. Sci.*, 2011, **4**, 1428.
13. H. G. S. Casalongue, M. L. Ng, S. Kaya, D. Friebel, H. Ogasawara and A. Nilsson, *Angew. Chem., Int. Ed.*, 2014, **53**, 7169.
14. J. B. Xu, P. Gao and T. S. Zhao, *Energy Environ. Sci.*, 2012, **5**, 5333.
15. F. Cheng, J. Shen, B. Peng, Y. Pan, Z. Tao and J. Chen, *Nat. Chem.*, 2011, **3**, 79.
16. X. Ge, Y. Liu, F. W. T. Goh, T. S. A. Hor, Y. Zong, P. Xiao, Z. Zhang, S. H. Lim, B. Li, X. Wang and Z. Liu, *ACS Appl. Mater. Interfaces*, 2014, **6**, 12684.
17. J. Suntivich, H. A. Gasteiger, N. Yabuuchi, H. Nakanishi, J. B. Goodenough and Y. Shao-Horn, *Nat. Chem.*, 2011, **3**, 546.
18. J. Suntivich, K. J. May, H. A. Gasteiger, J. B. Goodenough and Y. Shao-Horn, *Science*, 2011, **334**, 1383.
19. M. Risch, K. A. Stoerzinger, S. Maruyama, W. T. Hong, I. Takeuchi and Y. Shao-Horn, *J. Am. Chem. Soc.*, 2014, **136**, 5229.
20. J. I. Jung, H. Y. Jeong, J. S. Lee, M. G. Kim and J. Cho, *Angew. Chem., Int. Ed.*, 2014, **53**, 4582.
21. R. A. Rincon, E. Ventosa, F. Tietz, J. Masa, S. Seisel, V. Kuznetsov and W. Schuhmann, *ChemPhysChem*, 2014, **15**, 2810.
22. J. Sunarso, A. A. J. Torriero, W. Zhou, P. C. Howlett and M. Forsyth, *J. Phys. Chem. C*, 2012, **116**, 5827.
23. F. Bonaccorso, L. Colombo, G. Yu, M. Stoller, V. Tozzini, A. C. Ferrari, R. S. Ruoff and V. Pellegrini, *Science*, 2015, **347**, 6217.
24. H. Wang, M. Xie, L. Thia, A. Fisher and X. Wang, *J. Phys. Chem. Lett.*, 2013, **5**, 119.
25. D. S. Geng, Y. Chen, Y. G. Chen, Y. L. Li, R. Y. Li, X. L. Sun, S. Y. Ye and S. Knights, *Energy Environ. Sci.*, 2011, **4**, 760.

26. H. Wang, T. Maiyalagan and X. Wang, *ACS Catal.*, 2012, 2, 781.
27. D. P. He, K. Cheng, T. Peng, X. L. Sun, M. Pan and S. C. Mu, *J. Mater. Chem.*, 2012, **22**, 21298.
28. C. Zhang, R. Hao, H. Yin, F. Liu and Y. Hou, *Nanoscale*, 2012, **4**, 7326.
29. Y. Liang, Y. Li, H. Wang, J. Zhou, J. Wang, T. Regier and H. Dai, *Nat. Mater.*, 2011, **10**, 780.
30. Y. Y. Liang, Y. G. Li, H. L. Wang and H. J. Dai, *J. Am. Chem. Soc.*, 2013, **135**, 2013.
31. J. Kim, X. Yin, K.-C. Tsao, S. Fang and H. Yang, *J. Am. Chem. Soc.*, 2014, **136**, 14646.
32. J. J. Zhu and A. Thomas, *Appl. Catal., B*, 2009, **92**, 225.
33. A. Feldhoff, M. Arnold, J. Martynczuk, T. M. Gesing and H. Wang, *Solid State Sci.*, 2008, **10**, 689.
34. M. Liu, R. Wang, D. F. Li and D. T. Liang, *Mater. Chem. Phys.*, 2007, **102**, 132.
35. J. Blasco, J. García, J. M. de Teresa, M. R. Ibarra, J. Perez, P. A. Algarabel, C. Marquina and C. Ritter, *Phys. Rev. B*, 1997, **55**, 8905.
36. T. A. Tyson, Q. Qian, C. C. Kao, J. P. Rueff, F. M. F. de Groot, M. Croft, S. W. Cheong, M. Greenblatt and M. A. Subramanian, *Phys. Rev. B*, 1999, **60**, 4665.
37. C. Autret, J. Hejtmanek, K. Knizek, M. Marysko, Z. Jirak, M. Dlouha and S. Vratislav, *J. Phys.: Condens. Matter*, 2005, **17**, 1601.
38. M. C. Viola, M. J. Martínez-Lope, J. A. Alonso, J. L. Martínez, J. M. De Paoli, S. Pagola, J. C. Pedregosa, M. T. Fernández-Díaz and R. E. Carbonio, *Chem. Mater.*, 2003, **15**, 1655.
39. A. P. Sazonov, I. O. Troyanchuk, M. Kopcewicz, V. V. Sikolenko, U. Zimmermann and K. Baerner, *J. Phys.: Condens. Matter*, 2007, **19**, 046218.
40. J. Q. Yan, J. S. Zhou and J. B. Goodenough, *Phys. Rev. B*, 2004, **69**, 134409.
41. M. A. Korotin, S. Y. Ezhov, I. V. Solovyev, V. I. Anisimov, D. I. Khomskii and G. A. Sawatzky, *Phys. Rev. B*, 1996, **54**, 5309.
42. P. G. Radaelli and S. W. Cheong, *Phys. Rev. B*, 2002, **66**, 094408.
43. K. Asai, A. Yoneda, O. Yokokura, J. M. Tranquada, G. Shirane and K. Kohn, *J. Phys. Soc. Jpn.*, 1998, **67**, 290.
44. H. Berthou, C. K. Jørgensen and C. Bonnelle, *Chem. Phys. Lett.*, 1976, **38**, 199.
45. W. Y. Howng and R. J. Thorn, *J. Phys. Chem. Solids*, 1980, **41**, 75.
46. Z. H. Sheng, L. Shao, J. J. Chen, W. J. Bao, F. B. Wang and X. H. Xia, *ACS Nano*, 2011, **5**, 4350.
47. G. Wu, G. Cui, D. Li, P.-K. Shen and N. Li, *J. Mater. Chem.*, 2009, **19**, 6581.
48. T. Sharifi, G. Hu, X. Jia and T. Wagberg, *ACS Nano*, 2012, **6**, 8904.
49. O. Antoine and R. Durand, *J. Appl. Electrochem.*, 2000, **30**, 839.
50. X. Han, F. Cheng, T. Zhang, J. Yang, Y. Hu and J. Chen, *Adv. Mater.*, 2014, **26**, 2047.
51. Y. Gorlin and T. F. Jaramillo, *J. Am. Chem. Soc.*, 2010, **132**, 13612.
52. C. C. L. McCrory, S. Jung, J. C. Peters and T. F. Jaramillo, *J. Am. Chem. Soc.*, 2013, **135**, 16977.
53. W. G. Hardin, D. A. Slanac, X. Q. Wang, S. Dai, K. P. johnston and K. J. Stevenson, *J. Phys. Chem. Lett.*, 2013, **4**, 1254.
54. Y. Zhan, C. H. Xu, M. H. Lu, Z. L. Liu and J. Y. Lee, *J. Mater. Chem. A*, 2014, **2**, 16217.
55. N. Staud, H. Sokol and P. N. Ross, *J. Electrochem. Soc.*, 1989, **136**, 3570.